Journal of Sailing Technology 2019, volume 4, issue 1, pp. 66 - 83.
The Society of Naval Architects and Marine Engineers.

Velocity Prediction of Wing-Sailed Hydrofoiling Catamarans

Nils Hagemeister
Formerly University of Auckland, New Zealand, nhag107@aucklanduni.ac.nz

Richard G. J. Flay
University of Auckland, New Zealand, r.flay@auckland.ac.nz

Manuscript received January 1, 2018; revision received January 2, 2018; accepted January 3, 2018.

Abstract. The paper presents a Velocity Prediction Program for hydrofoiling catamarans with solid wing sails. Starting from a description of the mechanical model, suitable models are identified for the forces that act on the boat components. The study is deliberately limited to means for restricted methods where computational resources and budgets are limited. Enhanced lifting line approaches are described for the wingsail and appendages. Windage is calculated from force coefficients and dynamic pressure while hull resistance is determined by means of a potential flow solver. The description of the implementation is followed by the presentation of the results. An approach for processing of measurement data is shown in preparation to compare measured and predicted performance. Good agreement was found for upwind conditions whereas varying differences are found for most of the remaining wind angles. Finally, some of the challenges encountered during the study are discussed.

Keywords: Velocity Prediction Program, Hydrofoil, Wingsail, Performance Analysis

NOMENCLATURE

A	Reference area [m²]
AoA	Angle of attack [°]
AWS	Apparent wind speed [m s^{-1}]
BS	Boatspeed [m s^{-1}]
c_F	Coefficient of force [-]
c_L	Coefficient of lift [-]
c_i, $\vec{c_i}$	Local chord/chord vector [m]
d	Perpendicular distance between vortex filament and collocation point [m]
d_{core}	Diameter of viscous vortex core [m]
F	Force [N]
k	Vortex strength reduction factor [-]
M	Moment [N m]
$\vec{r}$	Vector between start of free vortex filament and collocation point [m]
Re	Reynolds number [-]
s_i, $\vec{s_i}$	Local span/span vector [m]
TWA	True wind angle [°]
TWS	True wind speed [m s^{-1}]
u	Incident flow velocity [m s^{-1}]
v_{indC}	Velocity induced at point P_C [m s^{-1}]
$\vec{v_i}$	Total induced velocity vector [m s^{-1}]
$\vec{v_{i,j}}$	Induced velocity vector [m s^{-1}]
$\vec{v_{mi,j}}$	Mirror image induced velocity vector [m s^{-1}]
$\vec{w_i}$	Total velocity vector [m s^{-1}]
z	Vertical distance [m]
z_C	Vertical collocation point position [m]

Γ Vortex strength [$m^3 s^{-1}$]
ρ Density of water/air [kg m^{-3}]

1. INTRODUCTION

A lot of the recent developments in high performance yacht design have focused on hydrofoiling and rigid wing sails. These technologies have been employed separately in sailing yachts for a long time, but were rarely combined in one boat. This eventually changed prior to the 34th America's Cup in 2013, which was contested in catamarans equipped with wings and appendages designed to promote foiling.

Similarly velocity prediction programs (VPPs) are widely used tools among yacht designers for the assessment of the speed potential of yachts. As a result of extensive development conducted during previous years, when the most prestigious regattas were sailed in monohulls, VPPs concerning this type of boat have become quite mature. However, experience shows that every VPP needs some degree of adaption to the type of boat under consideration. As multihulls have rarely gotten the attention of a wider audience prior to the 34th America's Cup, comparatively little work has been published on velocity prediction of catamarans. This effect is amplified by the fact that, because an accurate VPP represents a competitive advantage, sailing teams and design offices mostly keep their performance and VPP knowledge a secret.

2. FORCE DECOMPOSITION

The fundamental principle of each VPP is the equilibrium of forces and moments, as expressed in Eq.1.

$$\sum F = \sum M = 0, \tag{1}$$

Figure 1 illustrates the force decomposition applied in this study. The aerodynamic force is split into windage and rig forces in the longitudinal and transverse directions. The hydrodynamic forces are assembled from the contributions of the hull and appendages. The hull is affected by buoyancy and resistance while the appendages exert forces along all three axes on the boat.

As shown in Figure 1 the catamaran is modelled with the windward hull just above the water surface, since the righting moment is at its maximum in this state.

3. AERODYNAMIC FORCES

3.1 Windage

Windage forces are determined as the product of dynamic pressure $\frac{\rho}{2}\,AWS^2$and force coefficient c_{F} (Eq. 2), which is varied depending on the geometric characteristics of the object.

$$F_{\mathrm{i}}(z_{\mathrm{i}}) = c_{\mathrm{Fi}}\,\frac{\rho}{2}\,AWS(z_{\mathrm{i}})^2\,A_{\mathrm{i}}. \tag{2}$$

Windage items have been divided into three groups for this study. Cables and parts with circular cross sections and high length/diameter ratios operate in laminar flow (Fossati, 2009). These have been vertically segmented to take changes in apparent wind over height into account. Platform components like hulls and beams extend mainly parallel to the water surface are thus subject to a constant apparent wind speed and direction. Since the incident flow, dimensions and orientations of the remaining objects like the crew, winches and media equipment are somewhat unknown, they are modelled as 10% of the platform drag. Table 1 lists the groups and the associated force coefficients.

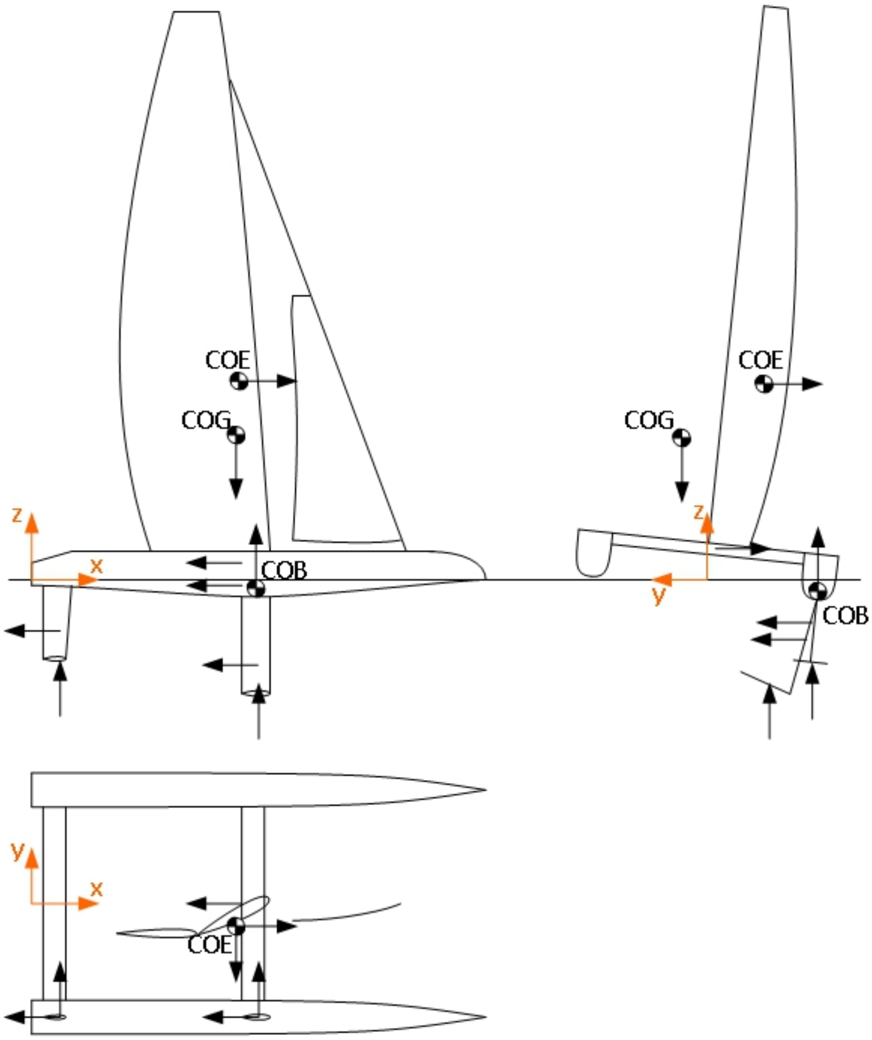

Figure 1. Force modelling of the catamaran.

Table 1. Windage item grouping.

Group	Description	cF [-]
cables	Circular cross sections & high length/diameter ratios (2D laminar flow)	1.1
platform	Parallel to waterplane (constant apparent wind)	0.6
misc.	Unknown remaining items	10% platform drag

3.2 Wing Forces

Graf *et al.* (2013) have shown that the forces developed by a wingsail can be accurately modelled by a modified lifting line method, which is briefly summarized below.

A bound vortex filament is created by expanding the lifting vortex from the Kutta-Joukowski theorem along the span of the wing. To comply with Thompson's law, the vortex filament is extended to infinity along the incident flow at the wing tips, forming a so-called horseshoe vortex.

Any change in lift can be represented by modifying the strength of the bound vortex and associated shedding of the differential vorticity through a free vortex filament. A vortex sheet is created by placing an infinite number of free vortex filaments between two reference points.

According to the Biot-Savart law, shed vorticity induces a velocity normal to incident flow and span that reduces the effective angle of attack. Figure 2 illustrates the discretization of the wing into panels.

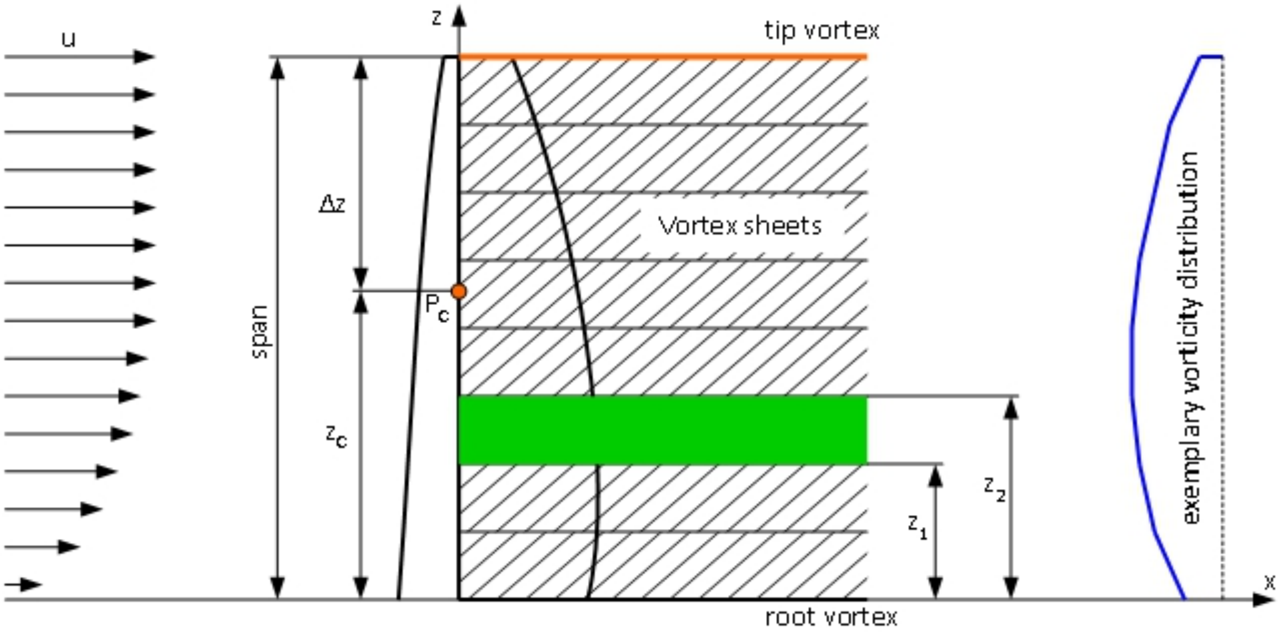

Figure 2. Wing discretization.

The total velocity induced in collocation point P_C can be calculated using Eq. 3 (Graf, et al., 2013), where v_{indC} denotes the velocity induced in the collocation point, Γ represents the vortex strength and z vertical coordinates according to Figure 2 above. Note that the strength of the root vortex is dampened by a factor EP to model end plate effects of the platform.

$$v_{\mathrm{indCj}} = \left[\sum_{\mathrm{i=1}}^{\mathrm{N,i\neq j}} -\frac{1}{4\pi}\frac{\Gamma_{\mathrm{i}}-\Gamma_{\mathrm{i-1}}}{z_{\mathrm{i}}-z_{\mathrm{i-1}}}\ln\left(\frac{z_{\mathrm{i}}-z_{\mathrm{Cj}}}{z_{\mathrm{i-1}}-z_{\mathrm{Cj}}}\right)\right] - \frac{1}{4\pi}\frac{\Gamma_0}{\left(z_0-z_{\mathrm{Cj}}\right)} + \frac{1}{4\pi}\frac{\Gamma_{\mathrm{N}}}{\left(z_{\mathrm{N}}-z_{\mathrm{Cj}}\right)}, \tag{3}$$

The vortex strength is derived from Eq. 4, where u and A are the apparent wind velocity and panel area, respectively. The lift coefficients c_{L} are interpolated as function of effective angle of attack $AoA - \frac{v_{\mathrm{ind}}}{u}$ and Reynolds number Re from tabulated data for the specific wing section

$$\Gamma = \frac{u}{2}\, A\, c_{\mathrm{L}}\left(AoA - \frac{v_{\mathrm{ind}}}{u}, Re\right). \tag{4}$$

Since Eqs. 3 and 4 depend on each other, the solution has to be found iteratively, for which under-relaxation is applied (Graf, et al., 2013). Once the effective angle of attack has been determined it can be used to look up the corresponding profile drag in a table.

4. HYDRODYNAMIC FORCES

4.1 Appendage Model

The appendages have been modelled using a three dimensional variant of the lifting line method. A detailed description of the method covering all details is given in (Flay & Hagemeister, 2017). A wing of arbitrary orientation is discretized with horseshoe vortices according to figure 3.

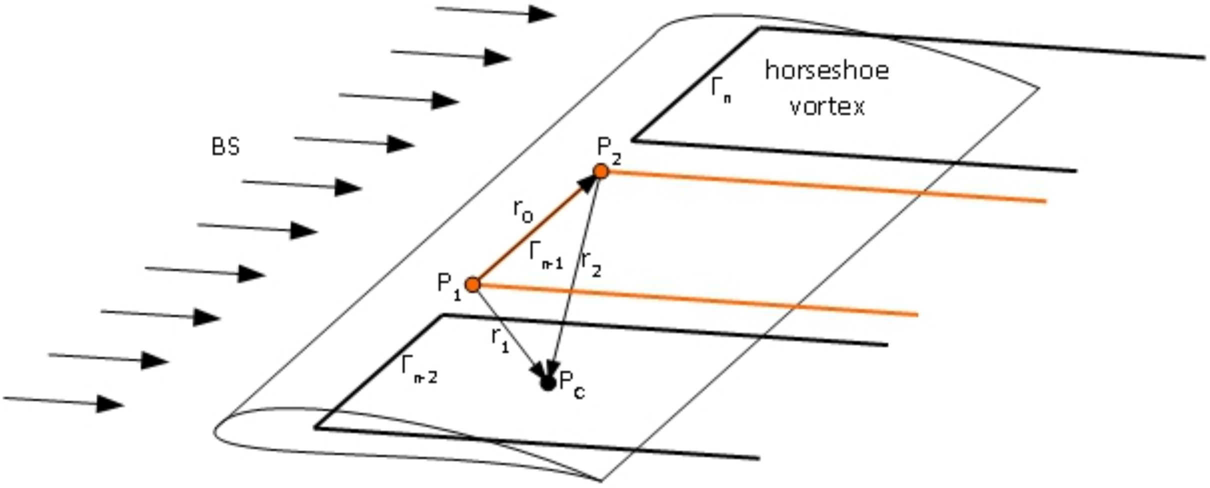

Figure 3. Discretization of appendages.

Phillips and Snyder derived the induced velocity vector $\overrightarrow{v_{\mathrm{i,n-1}}}$ generated by a horseshoe vortex with constant vortex strength $\Gamma_{\mathrm{n-1}}$ positioned along the ¼ -chord line as Eq.5 (Phillips & Snyder, 2000). In this equation $\overrightarrow{BS}$ represents the boatspeed vector and any $\vec{\mathrm{r}}$ is a vector from the start of a free vortex filament to collocation point P_c as shown in figure 3 above.

$$\overrightarrow{v_{\mathrm{i,n-1}}} = \frac{\Gamma_{\mathrm{n-1}}}{4\pi}\left[k_2 \frac{\left(\frac{\overrightarrow{BS}}{|\overrightarrow{BS}|}\times\overrightarrow{r_2}\right)}{|\overrightarrow{r_2}|\left(|\overrightarrow{r_2}|-\frac{\overrightarrow{BS}}{|\overrightarrow{BS}|}\cdot\overrightarrow{r_2}\right)} + k_0 \frac{(|\overrightarrow{r_1}|+|\overrightarrow{r_2}|)(\overrightarrow{r_1}\times\overrightarrow{r_2})}{|\overrightarrow{r_1}||\overrightarrow{r_2}|\,(|\overrightarrow{r_1}||\overrightarrow{r_2}|+\overrightarrow{r_1}\cdot\overrightarrow{r_2})} - k_1 \frac{\left(\frac{\overrightarrow{BS}}{|\overrightarrow{BS}|}\times\overrightarrow{r_1}\right)}{|\overrightarrow{r_1}|\left(|\overrightarrow{r_1}|-\frac{\overrightarrow{BS}}{|\overrightarrow{BS}|}\cdot\overrightarrow{r_1}\right)}\right] \tag{5}$$

The factors denoted k in Eq.5 above have been introduced to avoid the singularity in the Biot-Savart law through gradual reduction of the vorticity for vortex distances approaching zero. This effect enables a finer discretization of the wing to offset the reduced accuracy from bound vortices of constant strength compared to using vortex sheets as done for the wingsail. k is computed according to Eq. (6) from the perpendicular distance between vortex filament and collocation point d and the size of the viscous vortex core d_{core} (Abedi, 2013). Values of d_{core} = 0.01 m and m = 2 were selected for this study.

$$k = \frac{d^m}{(d_{core}^{2m} + d^{2m})^{\frac{1}{m}}} \tag{6}$$

The vortex strength is calculated according to Eq.7 where s_i and c_i represent the local span and chord and $\overrightarrow{s_\mathrm{i}}$ is the local chord vector.

$$\Gamma_\mathrm{i} = \frac{0.5\, BS^2\, s_\mathrm{i}\, c_\mathrm{i}\, c_{\mathrm{L_i}}(AoA_i, Re_i)}{|\overrightarrow{w_\mathrm{i}} \times \overrightarrow{s_\mathrm{i}}|}. \tag{7}$$

The total velocity $\overrightarrow{w_\mathrm{i}}$ is the sum of incident flow (boatspeed) and induced velocity as shown in Eq. 8.

$$\overrightarrow{w_\mathrm{i}} = \overrightarrow{BS} + \overrightarrow{v_\mathrm{i}}. \tag{8}$$

The angle of attack in each panel AoA_i is determined as per Eq. 9 (Phillips & Snyder, 2000) in which $\overrightarrow{q_\mathrm{i}}$ and $\overrightarrow{c_\mathrm{i}}$ denote the vectors normal to the wing surface and along the chord, respectively. In contrast to the 2D-variant described in section 3, this is the effective and not the geometric angle of attack.

$$AoA_\mathrm{i} = \tan^{-1}\left(\frac{\overrightarrow{w_\mathrm{i}} \cdot \overrightarrow{q_\mathrm{i}}}{\overrightarrow{w_\mathrm{i}} \cdot \overrightarrow{c_\mathrm{i}}}\right). \tag{9}$$

Summing up the individual contribution of all horseshoe vortices and their mirror images reflected at the water surface gives the total induced velocity, Eq.10. The mirroring cancels out the wing lift at the water surface.

$$\overrightarrow{v_\mathrm{i}} = \sum_{\mathrm{j=1}}^{\mathrm{n}} \overrightarrow{v_\mathrm{i,j}} + \sum_{\mathrm{j=1}}^{\mathrm{n}} \overrightarrow{v_\mathrm{mi,j}} \tag{10}$$

Emerged wing sections are modelled by setting their associated density to zero. Again profile drag is derived from tabulated data as function of angle of attack and Reynolds number. The rudder is modelled by superimposing the effects of two perpendicular wings.

4.2 Appendage Design

The appendages have been modelled according to figure 4. The winglet or tip section is joined to the daggerboard by a radial transition. The rudder assembly consists of two perpendicular wings. Although inspiration was drawn from the early AC72 daggerboard designs, the authors do not claim these designs to be particularly sophisticated.

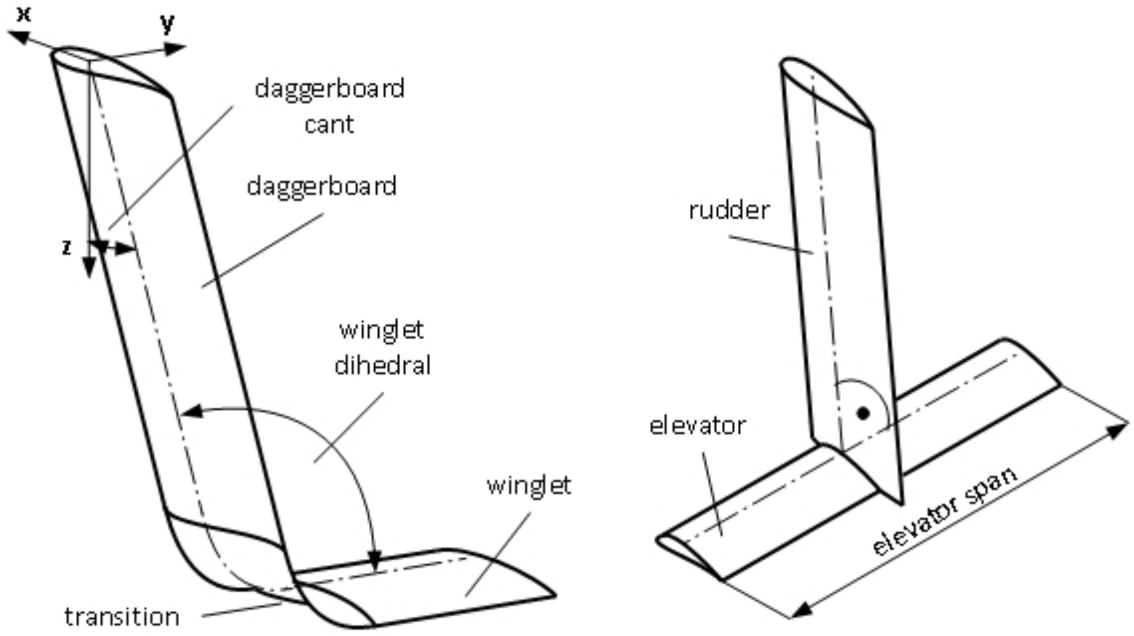

Figure 4. Geometry of appendages.

The selected dimensions are given in table 2.

Table 2. Appendage dimensions.

daggerboard chord	[m]	0.80
rudder chord	[m]	0.30
elevator chord	[m]	0.25
daggerboard span	[m]	3.50
transition segment	[m]	0.39
winglet span	[m]	1.25
rudder span	[m]	2.25
elevator span	[m]	1.25
daggerboard cant	[°]	10.00
winglet dihedral	[°]	90.00

4.3 Daggerboard Forces

The behaviour of the daggerboards has been analysed by Graf *et al.* (2016), who found the square of the total lift to be proportional to the drag. To investigate how the results of the lifting line method presented above compare to their RANS simulations, daggerboard forces were calculated for a similar test matrix. The results are presented in Figure 5. z_0 refers to the elevation of the yacht in relation to the still water plane. It can be seen that the results of the lifting line approach can indeed be approximated by a straight line, although there seems to be one outlier in each dataset. Due to the unavailability of the exact geometry for the reference case, the comparison was limited to a qualitative assessment. However, compared to the results of Graf *et al.* (not shown in figure) the drag forces seemed to be on the low side, which is attributed to the lack of wavemaking drag in the lifting line approach.

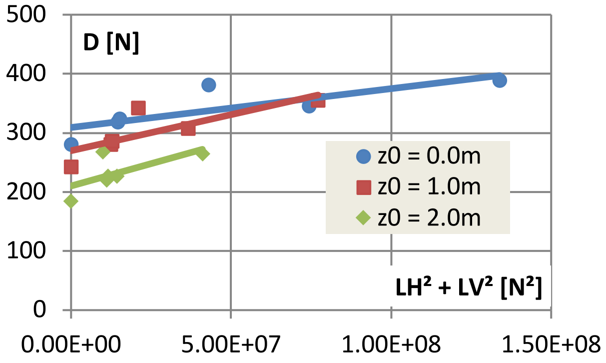

Figure 5. Daggerboard drag over lift squared as calculated by lifting line approach for $BS = 6$ m s^{-1}.

4.4 Hull Resistance

Following the suggestion of Oliver (1989), the wavemaking resistance of the hull is determined from the Michell formula, which is implemented in the MICHLET research code (Cyberiad, 2014). It is based on slender ship theory and is thus ideally suited for analysing sailing catamaran hulls. Frictional resistance is calculated as the product of static wetted surface area, dynamic pressure and friction coefficient derived from the ITTC’57 friction line.

The resistance predictions have been compared against towing tank test data of a TORNADO class hull. The results are presented in figure 6, which shows resistance as a function of Froude number. It can be seen that there is good agreement between both sets of data up to a Froude number of about 0.8. The wavemaking resistance hump around $Fn = 0.4$ is well captured. The increasing disparity can be explained by the lack of viscous pressure resistance in the prediction data. Since viscous pressure resistance is caused by friction, it is expected to be approximately proportional to frictional resistance.

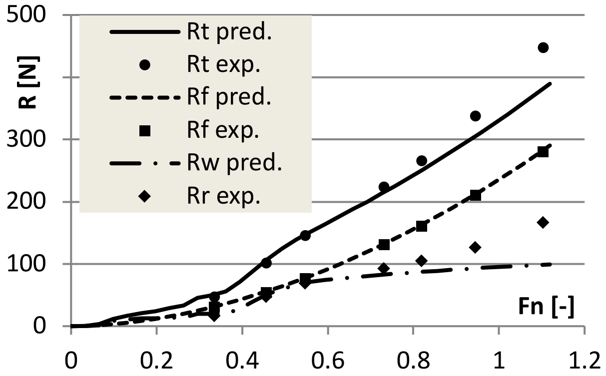

Figure 6. Comparison of predicted and experimental resistance data for a Tornado class hull.

5. IMPLEMENTATION

The VPP has been implemented as a constraint optimization routine in MATLAB. The optimization objective is maximum boatspeed. The constraints are supplied as a function to a steepest gradient algorithm. Every evaluation of the constraints function triggers function calls to determine the forces acting on each component for the current set of variables and only falls back to classic interpolation to obtain hull resistance and hydrostatics. To increase the solution speed, the result from the previous wind angle is used as the starting point for the current condition.

Forces and Moments are evaluated for all six degrees of freedom. Equilibrium is enforced for all components of translation and the moment about the vertical axis. Upper and lower limits are put in place for the heeling and trimming moments. The heeling moment boundaries result from the transversely moveable (crew) weight and the assumption of the windward hull being just clear of the water. The imbalance of the trimming moment is restricted through the position of the longitudinal centre of buoyancy for allowed trim extrema of ±1.5° at any given displacement. As a consequence, the trimming moment limits depend on the hydrostatic buoyancy force, which means that full equilibrium is enforced for the moment about the transverse axis for foiling states. Trim is not explicitly modelled, but is taken into account by varying the rudder elevator angle of attack, which then attains the meaning of a target trim plus elevator angle.

In total the VPP varies eight variables, which are listed in table 3 with their corresponding bounds. Twist is defined as angle differential between the root and tip sections of the wing and varies linearly in-between.

Table 3. Optimization variables with bounds.

Variable	Units	min.	max.
boatspeed	[m s^{-1}]	0	Infinity
sheeting angle	[°]	-10	Infinity
wing twist	[°]	0	45
rake	[°]	-10	10
leeway angle	[°]	-5	5
rudder angle	[°]	-5	5
elevation z_0	[m]	0	2.45
trim/elevator angle	[°]	-1.5	1.5

The rig was originally modelled as a single element wing and without the jib in this study due to a lack of data and to reduce complexity. However, Graf *et al.* (2016) found that the jib does add little if any additional driving force to the wing system for upwind sailing cases. Furthermore, Collie *et al.* (2015) stated that a multi-element wing was only superior in (light-wind) downwind sailing. Therefore, accurate force predictions can still be expected at least for upwind and reaching conditions from this much simplified model.

Lift and drag coefficients for the wing models described are specified in tables as functions of angle of attack and Reynolds number for a given 2D-profile section. As lifting line theory is based on the assumption of two dimensional flow, it is not suitable for modelling of separated flow which exhibits distinctive three dimensional features. To force the optimizer into the attached flow regime, the lift curves have been modified as shown in figure 7 to impose a higher penalty on stalled flow while retaining the curve smoothness necessary for stable interpolation.

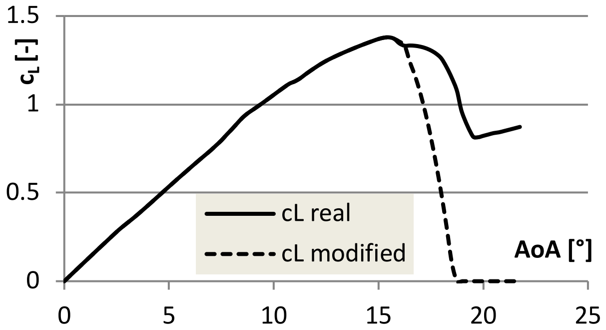

Figure 7. Example modified lift curve.

6. RESULTS

Figure 8 shows a polar plot of the velocities calculated by the VPP for true wind speeds (TWS) between 5.0 m s^{-1} and 12.5 m s^{-1} for an AC72 type yacht. Dimensions and design features were taken from the class rules and estimated from photographs. The continuous lines indicate the results for running the VPP from small to large wind angles with the dotted lines representing the reverse direction. It can be seen that speeds generally increase with the wind angle and wind speed as would be expected. Peak speeds are reached at a wind angle of about $TWA = 120°$. The transition to foiling can be spotted as a sudden distinctive increase in speed for all but the lowest windspeed. The angle for the beginning of foiling varies between $TWA = 60°$ and about $TWA = 75°$ with the lowest angle found for a windspeed of $TWS = 10.0$ m s^{-1}. It is not quite clear why the inception of foiling then goes back towards a higher angle for $TWS = 12.5$ m s^{-1}. However, as will be discussed later, this might be due to the aerodynamic modelling of the wing.

The dotted lines show the results for running the VPP in reverse, i.e. from large to small wind angles. It can be seen that around $TWA = 60°$ higher boatspeeds are predicted when turning upwind from higher wind angles.

It can be deduced that in this wind angle range the result depends on the initial state (foiling/non-foiling). However, this is not seen as a shortcoming since the exact same behaviour is expected for the real yacht as well. Because of the dependency of the foil's lift force on the velocity squared there is a minimum speed required for take-off. This speed has to be exceeded in floating mode where the hull adds considerably to the hydrodynamic resistance. This can be easily observed in Figure 9 which reveals the breakdown of the resistance forces before and after the transition to foiling for $TWS = 10.0$ m s^{-1}. The circular area indicates the total resistance. Once the hull is clear of the water its resistance component vanishes which manifests in a pronounced speed increase as can be seen in the polar plot. Furthermore, total resistance is actually reduced despite the elevated velocity. Hence, shortly after take-off the speed is considerably higher than the required take-off speed. As a result the foiling state can be maintained despite a reduction in speed when going to smaller wind angles.

It can also be noticed, that the lines plotted in the polar end at different true wind angles. This is due to the fact that the VPP has been run until no feasible solution was found anymore, which means that the optimizer was not able to find a solution that fulfils all equilibrium constraints. For downwind sailing this typically occurs, when the minimum heeling moment required to lift the windward hull out of the water cannot be reached anymore.

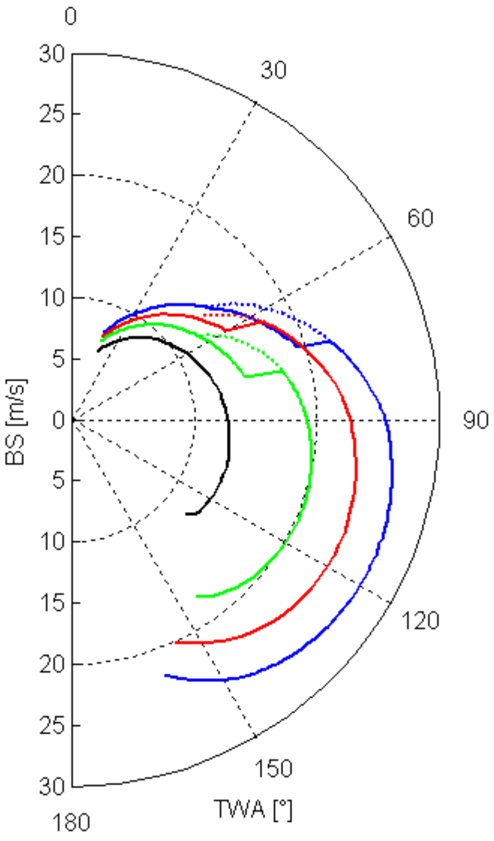

Figure 8. AC72 velocity polar for windspeeds of 5.0 m s^{-1} (black), 7.5 m s^{-1} (green), 10.0 m s^{-1} (red) and 12.5 m s^{-1} (blue).

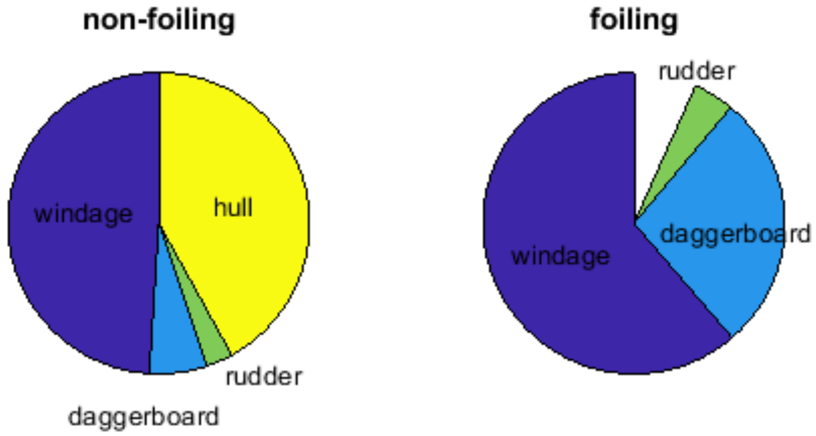

Figure 9. Resistance breakdown before and after transition to foiling at $TWS = 10.0$ m s^{-1}.

Figure 10 shows wing lift coefficient at $TWA = 60°$ plotted over height for the windspeeds known from the polar diagram. It was expected that the information could shed some light on why the foiling inception angle differs between the different wind velocities. It can be seen the maximum lift is always produced about 5.0 m above the wing root and then decreases with height. For the higher wind velocities it actually becomes negative which means righting moment is being generated by the top of the wing. It has to be noted that for wind speeds of 7.5 m s^{-1} and 10.0 m s^{-1}

the root section appears to be stalled. This is a result of the relatively low stall angle of the single element wing without jib. Usually effort is put into avoiding stall since it is associated with high drag. In this case however, it seems to be beneficial as the boat starts to foil earlier with a stalled root section at a TWS of 10.0 m s^{-1} than with the root section operating at a high lift coefficient at $TWS = 12.5$ m s^{-1}. Now this is probably an inaccuracy in the modelling of the wing aerodynamics, but it hints at the cause of why the boat starts foiling earlier at a lower wind velocity. The root of the wing sees the smallest apparent wind angles and therefore produces a predominantly lateral force which has to be balanced by the appendages. This increases the induced and probably also the profile drag of daggerboard and rudder, which might prevent foiling. In summary higher aerodynamic drag is traded for lower hydrodynamic drag.

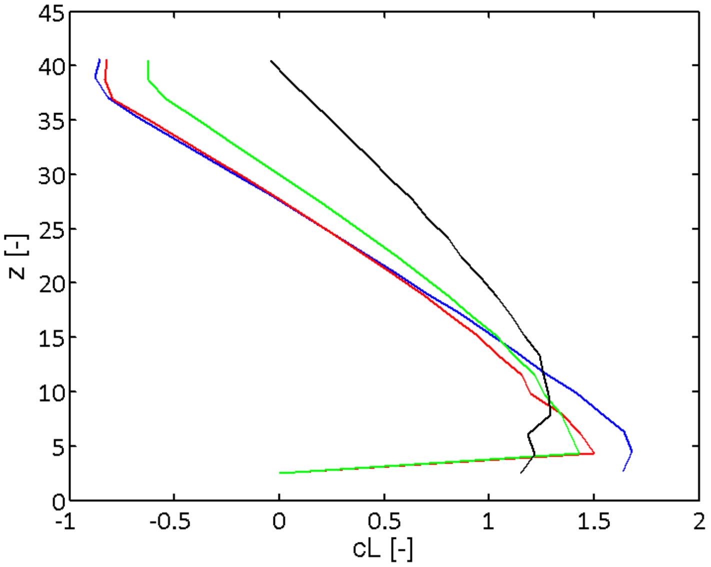

Figure 10. wing section lift coefficients plotted over height for $TWA = 60°$ and $TWS = 5.0$m s^{-1} (black), 7.5 m s^{-1} (green), 10.0 m s^{-1} (red), 12.5 m s^{-1} (blue).

A non-quantifiable result of this study was the observation of the stability of the VPP being influenced by the cant angle of the daggerboard. It was initially assumed that there is no difference in the optimization between a vertical daggerboard and one canted inwards by 10°. However, it was found that the VPP was finding equilibrium states much faster and more reliably with the canted board. This represents a nice analogy to what sailors and designers had experienced during the design of the actual daggerboards.

One of the challenges encountered during this study was the large number of variables to be optimized. The selection of variables has been a trade-off between realistic modelling and the ability to optimize reproducible parameters in a sensible amount of time. The number of adjustable parameters has been reduced considerably from what is found on actual boats. Examples of parameters that have remained fixed are daggerboard immersion and cant angle plus wing camber and trim angle, camber and twist of the headsail which has not been modelled. For future work it might be beneficial to separate optimization of trim settings and balancing of forces and moments through changes in for example leeway and rudder angle. However, since the balancing needs to be repeated for each combination of trim settings it remains to be seen if this actually increases the solution speed.

7. RACE DATA ANALYSIS & COMPARISON

Figure 11 shows plot of the velocity data recorded for ETNZ during the races of the 33rd America's Cup (America's Cup Event Authority/Sailing Yacht Research Foundation, 2013). It can be seen that the data is quite scattered and distributed unevenly over the true wind angles. In fact, two distinct bands of wind angles can be identified around which most of the data points are located, one around $TWA = 45°$ and one around $TWA = 150°$. While the first band stays approximately constant over all wind speeds, the true wind angles in the second band increase slightly with increasing wind speed. The boatspeed (indicated by the colour-bar) increases with the wind speed in both bands, with the highest velocities being reached in the area of $TWA = 150°$ and $TWS = 10.0$ m s^{-1}.

The two bands correspond approximately to the upwind and downwind VMG angles in the polar plot above (Figure 9). Since the races held were of the windward-leeward type, except from short reaching sections after the start and before the finish, the boats spent most of the racing time at these wind angles, explaining the data accumulation around them.

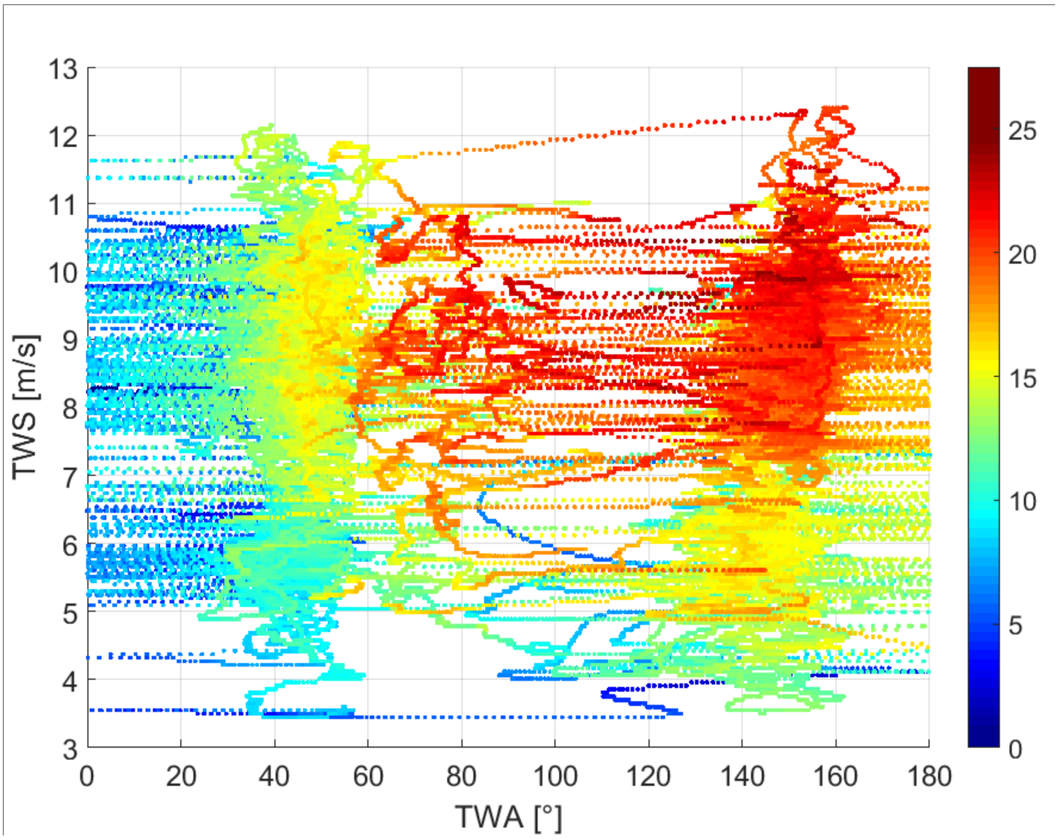

Figure 11. Velocity data of ETNZ AC72 recorded during 33rd America's Cup, boatspeed [m s^{-1}] according to colour bar.

For comparison between the predicted speeds and the recorded data, the measurements have been sorted into bins according to their associated true wind angle. Wind angle bins were chosen over wind speed bins, because the transition to foiling would create a discontinuity in almost all bins for the latter option whereas only few bins in the transition region are affected with wind angle bins. Each bin contains the values of all measurements within ±0.5° around each integer true wind angle. Since the boat velocity depends on the true wind speed, a second order polynomial fit through the origin has been performed for boatspeed as a function of wind velocity for each of the bins. An example of this is shown in Figure 12. This method was chosen to average out velocity fluctuations and reduce the impact of the omnipresent errors in measurement data. This was deemed necessary, because the measured speeds are calculated from distance and time between two successive positions. If the analysis was based purely on the best speed points a single inaccurate position would have a large impact on the result. Furthermore, since only race data has been analysed it was expected that the boat was close to optimal performance all of the time, which in theory means all data points should lie on a single line, which is clearly not the case.

While the sorting into narrow bins at least in principle allows the capturing of the transition into foiling mode for variations in TWA, the polynomial fit cannot capture this discontinuity for the boatspeed as a function of TWS. This is seen as a major deficit as it means that velocity will be over predicted for non-foiling states and under predicted for foiling states as the transition between the two is averaged out.

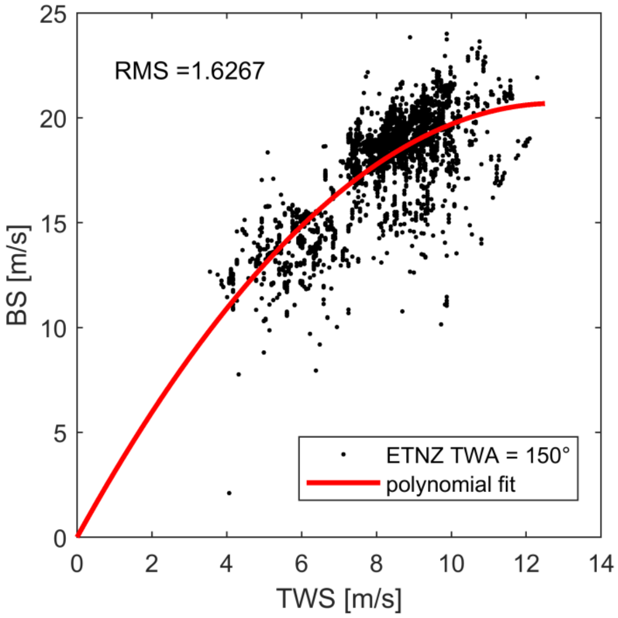

Figure 12. Polynomial fit of boatspeed over true wind speed for $TWA = 150°\pm0.5°$.

The quality of each curve fit has been examined by calculating the root mean square (RMS) to measure the spread of the recorded boatspeed data about the fitted curve.

A plot of the RMS values over TWA is shown in Figure 13. As can be seen the average deviation of the measurements to the fit varies between approximately 1.5 m s^{-1} and 3.5 m s^{-1}, which represents a significant percentage of the absolute boatspeed, which is predicted to reach a maximum of 25.0 m s^{-1}. This means that the significance of the data derived using the fits will be very limited.

Examining the plot more closely, it can be observed that there are two distinct sections of comparatively low RMS values. The first is located just under $TWA = 50°$ and the second starts at roughly $TWA = 145°$ and continues to $TWA = 180°$. These sections correspond well with the bands of high data density associated with the upwind and downwind VMG sailing angles observed in Figure 11.

Considering the deficits of the method mentioned above and the quality of the fit, only the data derived for the upwind and downwind sailing can be expected to bear any kind of statistical significance at best.

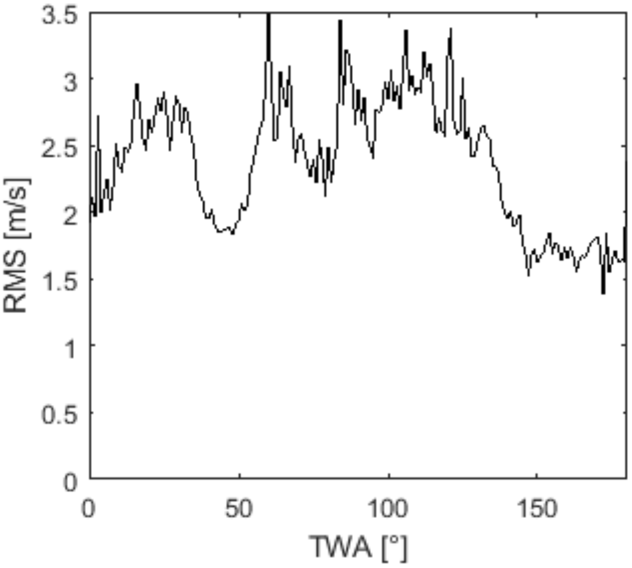

Figure 13. RMS of polynomial fits over TWA.

Despite the known severe limitations, the polynomials which result from the curve fits have been evaluated at the same true wind speeds for which the velocity prediction has been performed, to see if at least some general trends can be identified. The resulting velocities are plotted as function of TWA in Figure 14. Because of the relatively low amount of measurement data around $TWS = 12.5$ m s^{-1}, the presented analysis did not yield meaningful data for this wind speed, which has subsequently been spared from the plot.

It can be seen that for each wind speed there is a velocity for sailing straight into the wind, which can be explained by the mass momentum being carried through tacks. The minimum speed during tacks ranges from about 6.0 m s^{-1} to 7.5 m s^{-1} and remains roughly constant for the range $0 < TWA < 20°$. When higher wind angles are reached the speeds start to increase and differences between the true wind speeds start to materialize. As would be expected the lowest velocities are found for the lowest wind speed and vice versa. The boat speeds continue to increase until a TWA of just below 60° is obtained. At this angle a steep increase in velocity can be observed at all wind speeds, which is attributed to the transition into foiling mode. After the transition to foiling the speeds seem to remain relatively stable for $TWS = 5.0$ m s^{-1} and $TWS = 7.5$ m s^{-1}, although it has to be kept in mind that the scatter and the RMS are high in the range between $TWA = 60°$ and $TWA = 120°$. The curve for $TWS = 10.0$ m s^{-1} shows some areas of elevated speeds between $TWA = 80°$ and $TWA = 130°$, but the resulting discontinuities in the curve would neither be expected in a typical velocity polar nor from the prediction presented above. After passing $TWA = 150°$ the boatspeed starts to decrease at approximately the same rate for all three series, as the velocity offsets remain roughly constant. Again, it has to be expected that the effects of mass momentum being carried through a jibe are contained in the data for TWA around 180°.

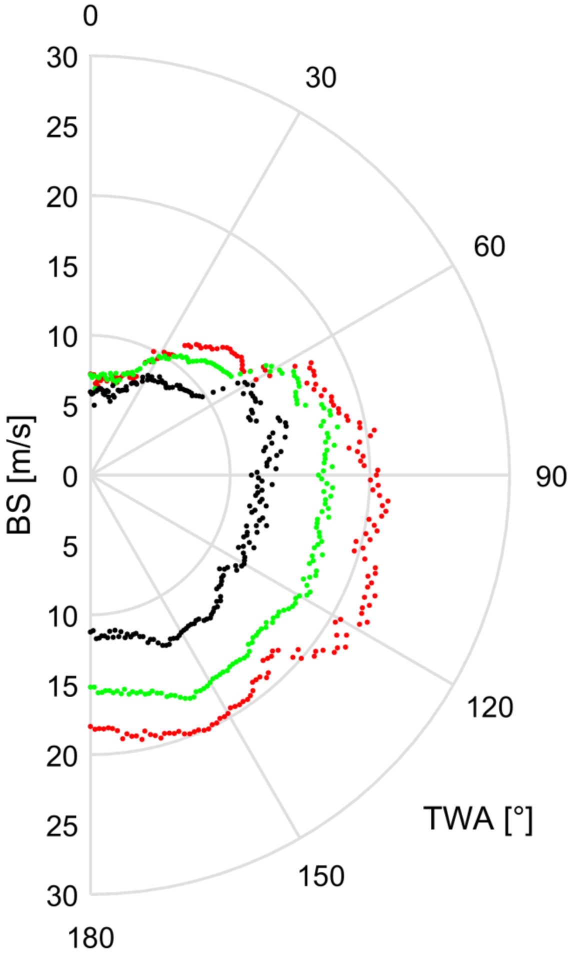

Figure 14. Measured AC72 velocity polar for windspeeds of 5.0 m s^{-1} (black), 7.5 m s^{-1} (green) and 10.0 m s^{-1} (red).

Figure 15 shows an overlay of the predicted performance and the data derived from the race recordings. It can be observed that the agreement between the datasets is fair for small wind angles between $TWA = 20°$ and $TWA = 60°$. As described above the measured data indicates a transition to foiling at this wind angle for all TWS. Of the predicted data only the red curve ($TWS = 10.0$ m s^{-1}) shows the transition to foiling at roughly the same wind angle. For $TWS = 7.5$ m s^{-1} this point is forecast at a much higher wind angle, whereas for 5.0 m s^{-1} the vessel is not expected to reach the foiling state. Consequently, the speed seems to be severely under predicted for those windspeeds at TWA above 60°. The prediction for 5.0 m s^{-1} then closes in on the measurement at about $TWA = 90°$ whereas the other curves exhibit significant over prediction of the velocity over most of the TWA range until they converge again with the measurement data approximately at the point of maximum downwind VMG.

The missing ($TWS = 5.0$ m s^{-1}) or delayed ($TWS = 7.5$ m s^{-1}) prediction of the take-off point might be caused by a lack of aerodynamic thrust force due to the simplified wing model. This is also seen as the reason for the lack of downwind speed/power at $TWS = 5.0$ m s^{-1} which was expected from findings in previous studies as described in section 5 above.

The main cause for the over prediction of speed is seen in the lack of wavemaking resistance in the appendage force models. However, most of the disagreement is found in a range where on one hand the quality of the data analysis suffers from a limited statistical basis and on the other hand the yacht was not sailing at one of the two wind angles for which straight line sailing at constant speed would be expected. Thus, the possibility remains that the yacht was mostly manoeuvring and thus not sailing at peak performance when sailing at these angles. The fluctuations in measured speed between $TWA = 90°$ and the distinct maxima at the downwind VMG angles, which can be observed in the data, support this theory as they would not be expected based on the velocity prediction, which shows a smooth curve over this range of wind angles.

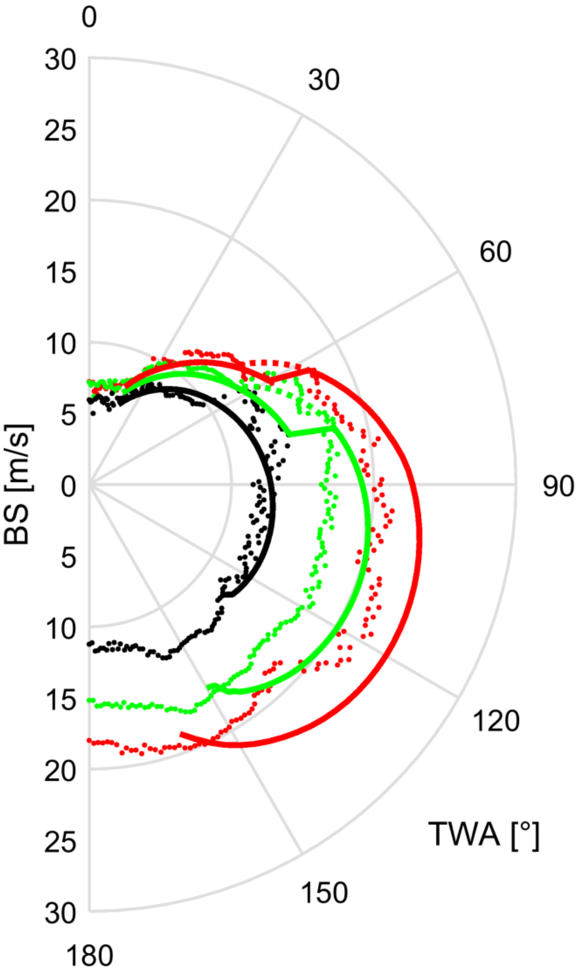

Figure 15. Measured (scatter) and predicted AC72 velocity polars and for windspeeds of 5.0 m s^{-1} (black), 7.5 m s^{-1} (green) and 10.0 m s^{-1} (red).

8. CONCLUSIONS

A VPP for performance prediction of wing-sailed catamarans has been developed. The transition between floating and foiling states can be captured. Including the jib in the aerodynamic wing model and adding wave resistance for the appendages is expected to improve the results of the lifting line methods. Furthermore, a second wing element could be added through supplying the corresponding data in the lift and drag tables. Measured performance data has been analysed. The method presented herein catches some key characteristics of the AC72 performance polar. However, the scattering of the measurement data compromises the validity of the absolute velocity values.

REFERENCES

Abedi, H., 2013. Development of Vortex Filament Method for Aerodynamic Loads on Rotor Blades, PhD Thesis, Chalmers University of Technology, Department of Applied Mechanics, Sweden.

America's Cup Event Authority/Sailing Yacht Research Foundation, 2013. Sailing Yacht Research Foundation : 34TH AMERICA'S CUP - LIVELINE DATA. [Online] Available at: http://www.sailyachtresearch.org/resources/34th-americas-cup-liveline/ [Accessed 6 April 2017].

Collie, S., Fallow, B., Hutchins, N. & Youngren, H., 2015. Aerodynamic Design Development of AC72 Wings. Proceedings of 5th High Performance Yacht Design Conference. Auckland, NZ.

Cyberiad, 2014. MICHLET 9.32 User's Manual, provided with the Michlet 9.32 Research Code which can be downloaded from http://www.cyberiad.net/michlet.htm.

Flay, R. & Hagemeister, N., 2017. Computational Techniques used in the Velocity Prediction of Wing-sailed, Hydrofoiling Catamarans. Proceedings of VII International Conference on Computational Methods in Marine Engineering VII MARINE 2017. Nantes, France, International Center for Numerical Methods in Engineering (CIMNE), pp. 312-323.

Fossati, F., 2009. Aero-Hydrodynamics And The Performance of Sailing Yachts. Adlard Coles Nautical ,London, UK.

Graf, K., Renzsch, H. & Meyer, J., 2016. Prediction and Optimization of Aerodynamic and Hydrodynamic Forces and Boat Speed of Foiling Catamarans with a Wing Sail and a Jib. Proceedings of the the 22nd Chesapeake Sailing Yacht Symposium. Annapolis, Maryland, USA.

Graf, K., van Hoeve, A. & Watin, S., 2013. Comparison of Full 3D-RANS Simulations with 2D-RANS/Lifting Line Method Calculations for the Flow Analysis of Rigid Wings for High Performance Multihulls. Proceedings of 3rd International Conference on Innovation in High Performance Sailing Yachts. Lorient, France.

Oliver, C., 1989. Performance Prediction Method for Multihull Yachts. Proceedings of the 9th Chesapeake Sailing Yacht Symposium. Annapolis, Maryland, USA, pp. 119-132.

Phillips, W. & Snyder, D., 2000. Modern adaption of Prandtl's classic lifting line theory. *Journal of Aircraft,* Vol. 37, No. 4, pp. 662-670.